

Fiducial Marker Splatting for High-Fidelity Robotics Simulations

Diram Tabaa Gianni Di Caro
Carnegie Mellon University
{dtabaa, gdicaro}@andrew.cmu.edu



Figure 1. Proof-of-concept greenhouse environment constructed from 2D Gaussian splats trained on cucumber greenhouse images. Our fiducial markers, generated without prior splatting-based training, are placed within the scene to support high-fidelity robotics simulation.

Abstract

High-fidelity 3D simulation is critical for training mobile robots, but its traditional reliance on mesh-based representations often struggle in complex environments, such as densely packed greenhouses featuring occlusions and repetitive structures. Recent neural rendering methods, like Gaussian Splatting (GS), achieve remarkable visual realism but lack flexibility to incorporate fiducial markers, which are essential for robotic localization and control. We propose a hybrid framework that combines the photorealism of GS with structured marker representations. Our core contribution is a novel algorithm for efficiently generating GS-based fiducial markers (e.g., AprilTags) within cluttered scenes. Experiments show that our approach outperforms traditional image-fitting techniques in both efficiency and pose-estimation accuracy.

We further demonstrate the framework’s potential in a greenhouse simulation. This agricultural setting serves as a challenging testbed, as its combination of dense foliage, similar-looking elements, and occlusions pushes the limits of perception, thereby highlighting the framework’s value

for real-world applications.

1. Introduction

Autonomous mobile robots have been increasingly adopted in real-world scenarios over the past few years. This adoption has been seen in diverse fields such as logistics [10, 44], manufacturing [14, 39], and agriculture [17, 46]. A central theme across all these applications are traditional mobile robotics challenges, including mapping and localization [8, 31], path planning [21, 26, 36], and navigation [13, 37]. Due to safety and cost constraints, these problems are typically first addressed in a simulated environment prior to real-world testing, which gives simulation a central role in robotics research.

Accordingly, robotic simulation environments have evolved substantially. In particular, 3D simulators like Gazebo [20] have improved the ability to test robotic solutions by emulating real-time visual input from the environment, whether in the form of RGB images, LiDAR data or depth maps. This modeling commonly relies on using 3D meshes to represent objects (e.g. chairs, walls) which are

manually created using CAD software [42, 43] or through 3D reconstruction methods [3, 45]. In agriculture, such simulators have been used to model robotic tasks in greenhouses [16, 40] and open fields [38].

Although mesh-based methods have expanded the scope of robotics simulation, they still lack sufficient realism. This is due to the reduced face count needed for real-time emulation and the nonrealistic imagery produced by raster-based methods. Although increased computational power from consumer graphics hardware has led to solutions such as real-time ray tracing, a core issue with mesh-based methods remains the effort required to produce these meshes. This is especially true for objects with complex geometries, such as plants and trees, whether through manual design or procedural algorithms. Recent generative AI models for 3D mesh generation, such as MeshGPT [35] and MeshDiffusion [25], are still incapable of accurately modeling complex non-convex structures.

Recent breakthroughs in radiance field rendering have enabled models that can faithfully capture real-world scenes using only a collection of reference images. Specifically, 3D Gaussian Splatting [18] allows for the creation of realistic radiance fields that can be rendered in real time and support inference from novel camera poses not included in the training set. These advances have led to widespread adoption in robotics simulation [5, 23, 47] because of their ability to model unconstrained, true-to-life scenes. However, the novelty of this representation means that little work has been done to integrate classical scene elements into radiance fields. This limitation impacts certain applications, particularly those involving fiducial markers, which are critical for localization in complex environments.

In this paper, we introduce a novel approach to using Gaussian Splatting in robotics simulation. We demonstrate the ability to integrate elements of classic robotics simulation into Gaussian Splatting representations by presenting a new algorithm to generate fiducial markers using Gaussian primitives. We show that this method outperforms classic Gaussian Splatting fitting approaches in both efficiency and the visual quality of the generated markers. To validate our framework, we present a proof-of-concept simulation in a greenhouse environment explicitly addressing localization tasks. This agricultural setting was chosen specifically as it represents a challenging domain with dense clutter and visual ambiguity, highlighting the potential of our framework to enable realistic and flexible simulation for a broad range of robotics research. Our contributions are threefold:

- We present a universal fiducial marker representation based on Gaussian primitives and a novel algorithm to generate these markers.
- We show that our algorithm outperforms standard Gaussian Splatting approaches in both efficiency and recognizability.

- We demonstrate the application of this framework to agricultural robotics simulations through a proof-of-concept.

2. Related Work

Our discussion of related work is divided into two sections to provide context for the core motivations behind our contributions. In 2.1, we review current work in radiance field rendering and highlight the need for a framework that can generate visual elements, such as fiducial markers, without prior training. Subsequently, 2.2 surveys existing agricultural simulation environments, showing how our work is motivated by the need to combine the photorealistic rendering of radiance field methods with the comprehensive capabilities of robotics simulation.

2.1. Radiance field rendering

Radiance fields model scenes as continuous functions that describe how light rays emanate from objects in a scene. Classical methods [11, 22] represented images as slices of the radiance field, but these approaches required a large number of images for reconstruction. NeRF [27] introduced a breakthrough by parameterizing radiance fields with neural networks, thereby reducing storage requirements by leveraging the inference capability of trained models. Subsequent work [1, 2, 28] focused on improving NeRF in terms of resolution and rendering speed, but these methods remained constrained by the computational cost of volumetric sampling. More recently, 3D Gaussian Splatting (3DGS) [18] addressed this limitation by representing radiance fields with Gaussian primitives that can be efficiently rasterized, enabling real-time radiance field rendering. Building on this idea, methods such as 2D Gaussian Splatting [15] and SuGaR [12] extended 3DGS to achieve more accurate surface modeling.

Despite these advances, radiance field methods still require per-scene training, which is not only time-consuming but also highly sensitive to input sparsity and camera pose accuracy. PixelSplat [4] mitigates this issue by pretraining a network to infer Gaussian primitives directly from two images in a single feed-forward pass. MVSplat [6] extends this approach to multiple sparse input images. However, these methods still depend on large-scale pretraining and, more importantly, assume a general setting where the target scene function is unknown. To the best of our knowledge, no prior work has addressed this challenge for simple geometric elements in a reconstruction-independent manner, which is particularly relevant in the context of fiducial markers.

2.2. Simulation in Agricultural Robotics

The simulation of botanical entities, a cornerstone of using simulation in modern agricultural robotics, has a rich history in computer graphics. The field was pioneered by procedural, rule-based methods, most notably the L-system

introduced by Lindenmayer [24]. Originally a model for cellular development, the L-system’s recursive grammar proved highly effective at simulating the branching growth patterns of plants. While foundational, the deterministic nature of early L-systems struggled to capture the inherent randomness of natural forms.

This limitation spurred the development of alternative procedural techniques, including the use of fractals to generate self-similar structures [30] and particle systems to model dynamic elements like leaves and blossoms [33]. A different school of thought moved beyond pure proceduralism, with some researchers focusing on creating models grounded in detailed botanical measurements [7], while others prioritized plausible visual realism over strict biological accuracy, as demonstrated by Weber et al. [41], who used parameterized conic structures to create realistic trees. These foundational techniques established the diverse approaches to plant modeling that underpin the high-fidelity simulators used today.

In the robotics context, simulators such as Gazebo mostly rely on mesh-based environment modelling, either curated by manual creation of CAD models or by utilizing procedural algorithms to automatically create them. In the specific agricultural context, GroIMP [19] and OpenAlea [32] presented open-source frameworks for procedural generation of 3D plant meshes. Although those frameworks provided flexibility to generate heterogeneous collections of plant meshes, they are still limited by the scope of manually adjusted generation parameters. In addition, while such models have been used in robotics simulation for tasks like navigation, they are rarely useful when it comes to creating realistic simulation environments that enable sim-to-real transfer, especially in vision-based tasks, such as fruit identification and counting.

3. Fiducial Marker Splatting

In this section, we introduce our method for representing fiducial markers with Gaussian primitives without relying on prior splatting-based training. The section is organized into three parts. First, we briefly describe the specific representation employed (2DGS). Second, we show how rectangles can be approximated with Gaussian primitives. Finally, we demonstrate how fiducial markers can be decomposed into a minimal set of primitives for compact representation.

3.1. Preliminary: 2D Gaussian Splatting

2D Gaussian Splatting (2DGS) [15] is a method for modeling and reconstructing geometrically accurate radiance fields from multi-view images. The core idea of 2DGS is to represent the 3D scene as a collection of 2D oriented planar Gaussian splats (i.e. ellipses). Unlike 3D Gaussians, these 2D primitives provide a more view-consistent geometry and are intrinsically better for representing surfaces. Each 2D

Gaussian primitive is defined by a set of parameters: a center point \mathbf{p}_k , two principal tangent vectors \mathbf{t}_u and \mathbf{t}_v which define the orientation of the ellipse in the 3D space, and two scaling factors, s_u and s_v , which control the variance or shape of the elliptical splat. Additionally, each primitive has an associated color \mathbf{c}_k and opacity α_k .

The final color of a pixel is rendered by alpha blending the 2D Gaussian primitives that project onto it. The primitives are sorted from front to back along the viewing ray. The color C for a pixel is computed by the following alpha blending formula:

$$C = \sum_{k \in K} c_k \alpha'_k \prod_{j=1}^{k-1} (1 - \alpha'_j)$$

where K is the set of sorted Gaussian indices, c_k is the color of the k -th Gaussian, and α'_k is the opacity of the k -th Gaussian modulated by its Gaussian function evaluated at the pixel location. This formulation allows for differentiable rendering, which is key for optimizing the parameters of the Gaussian primitives to reconstruct the scene.

3.2. Gaussian Approximation of Fiducial Markers

Piecewise-constant planar marker. Rectilinear fiducial markers (e.g., AprilTags [29]) admit a decomposition into axis-aligned rectangles in a local planar coordinate frame. This yields a closed-form, piecewise-constant function from coordinates to grayscale intensity.

Let $\{R_i\}_{i=1}^n$ be pairwise-disjoint, axis-aligned rectangles whose union defines the marker domain $\Omega \subset \mathbb{R}^2$:

$$R_i = [a_i^x, b_i^x] \times [a_i^y, b_i^y], \quad (1)$$

$$R_i \cap R_j = \emptyset \quad \forall i \neq j, \quad (2)$$

$$\bigcup_{i=1}^n R_i = \Omega. \quad (3)$$

Define $M : \Omega \rightarrow [0, 1]$ (grayscale) by

$$M(\mathbf{x}) = \sum_{i=1}^n c_i \chi_{R_i}(\mathbf{x}), \quad (4)$$

where $c_i \in [0, 1]$ and

$$\chi_{R_i}(\mathbf{x}) = \begin{cases} 1, & \mathbf{x} \in R_i, \\ 0, & \text{otherwise.} \end{cases} \quad (5)$$

Smooth approximation for 2D Gaussian splatting. To obtain a differentiable representation suitable for 2D Gaussian splatting (2DGS), we approximate each χ_{R_i} with a finite mixture of anisotropic 2D Gaussians that concentrate mass near rectangle edges while retaining a solid interior.

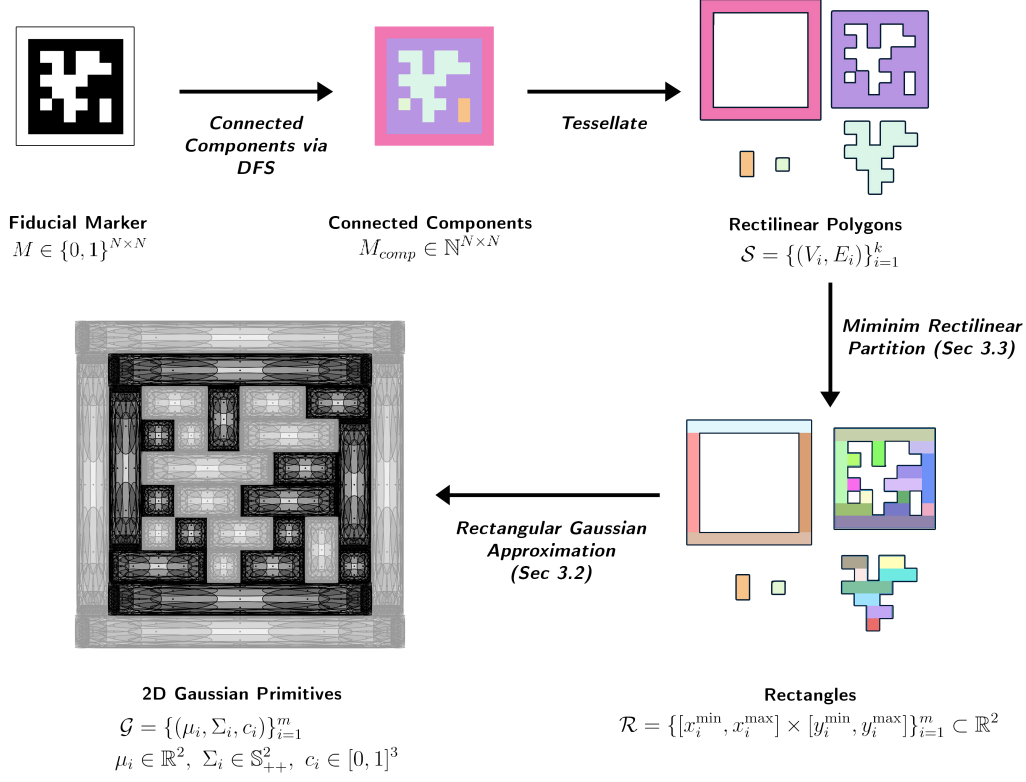


Figure 2. **Overview of the fiducial marker splatting pipeline.** A binary marker is first partitioned into connected components via DFS, which are then tessellated into rectilinear polygons. Each polygon is processed with the minimal rectilinear partition algorithm (Sec. 3.3) to obtain rectangles. These rectangles are then parameterized and converted into rectangular Gaussian approximators (Sec. 3.2), yielding the final set of 2D Gaussian primitives.

Consider a rectangle with center $c \in \mathbb{R}^2$, half-sizes $s_x, s_y > 0$, refinement levels $L \in \mathbb{N}$, and density modifier $\rho \geq 1$.

Level 0 (interior seed). Place a single anisotropic Gaussian at the center:

$$\mu_0 = c, \quad (6)$$

$$\Sigma_0 = S_0 S_0^\top, \quad S_0 = \text{diag}\left(\frac{s_x}{\gamma}, \frac{s_y}{\gamma}\right), \quad (7)$$

with $\gamma = 3.0$ serving as the 2DGS render cutoff hyperparameter.

Levels $l = 1, \dots, L - 1$ Define the level-dependent offset

$$d_l = (s_x(1 - 2^{-l}), s_y(1 - 2^{-l})), \quad (8)$$

and the first-quadrant “corner” point $p_l = c + d_l$. Place a corner Gaussian at p_l with

$$\mu_l = p_l, \quad (9)$$

$$\Sigma_l = \text{diag}(\sigma_{xl}^2, \sigma_{yl}^2), \quad (10)$$

where

$$\sigma_{xl} = \frac{s_x}{\gamma 2^l}, \quad \sigma_{yl} = \frac{s_y}{\gamma 2^l}. \quad (11)$$

Arms toward the corner. Populate two orthogonal arms meeting at p_l :

- **Horizontal arm:** place 2^{l-1} Gaussians with means $\mu_i = (c_x + o_i^x, c_y + d_{ly})$ where $o_i^x \in [0, d_{lx})$ are uniformly spaced, and covariances $\Sigma_i = \text{diag}(\sigma_{\parallel,i}^2, \sigma_{\perp,l}^2)$ with $\sigma_{\parallel,i} = (s_x - o_i^x)/\gamma$ and $\sigma_{\perp,l} = \sigma_{yl}$.
- **Vertical arm:** symmetrically, place 2^{l-1} Gaussians with means $\mu_j = (c_x + d_{lx}, c_y + o_j^y)$ where $o_j^y \in [0, d_{ly})$, and covariances $\Sigma_j = \text{diag}(\sigma_{\perp,l}^2, \sigma_{\parallel,j}^2)$ with $\sigma_{\parallel,j} = (s_y - o_j^y)/\gamma$ and $\sigma_{\perp,l} = \sigma_{xl}$.

Mirror the first-quadrant set across the axes through c to populate all four sides at level l . The final mixture aggregates components from levels $l = 0, \dots, L - 1$. To ensure a visually solid interior, upweight early-level components by a factor ρ (equivalently, replicate them ρ times).

Category	String Length	QR Version	Dimensions (px)
Small	20	2	25×25
Medium	100	5	37×37
Large	250	10	57×57
Huge	1000	22	105×105

Table 1. QR Code categories based on string length and corresponding QR versions.

3.3. Rectangular Partitioning of Fiducial Markers

As discussed in the previous subsection, reducing the number of 2D Gaussian primitives at the level of individual rectangles is essential to prevent performance degradation. Beyond this, additional optimization can be achieved at the scale of the entire marker. In particular, the primitive count can be reduced by minimizing the number of rectangles generated during partitioning, since fewer, larger rectangles eliminate redundant inner edges.

To accomplish this, the fiducial marker is first partitioned into connected components via Depth First Search (DFS) based on pixel color values. Each connected component is then converted into a rectilinear polygon, potentially with holes. For each rectilinear polygon, the minimal rectilinear partition algorithm of Ferrari et al. [9] is applied. This algorithm identifies the largest independent set of non-intersecting, axis-parallel concave vertex chords, partitions the polygon accordingly, and then further partitions any remaining concave vertices, which are guaranteed not to connect to one another after the initial step. A detailed description of the algorithm is provided in the Appendix. Finally, the resulting rectangles are parameterized by their center coordinates and s_x, s_y scales, yielding the rectangular approximators introduced in Section 3.2. The overall pipeline is illustrated in Figure 2.

4. Experiments

4.1. Experimental Setup

Datasets. Since no prior work exists on this problem, an evaluation dataset was constructed using AprilTags [29] and QR Codes. For AprilTags, five tags were selected from the 36h11 standard. For QR Codes, five tags were generated for each size category, where the size was determined by the length of randomly generated fixed-length strings, as defined in Table 1. To obtain the camera poses required for 2DGS training, four distinct viewpoint collections were designed (Figure 3) in order to evaluate the sensitivity of the baseline to viewpoint quality. Combining the generated tags with these viewpoint sets resulted in 20 trainable scenes for AprilTags and 80 for QR Codes, for a total of 100 distinct scenes stored in COLMAP [34] format. Finally, Blender

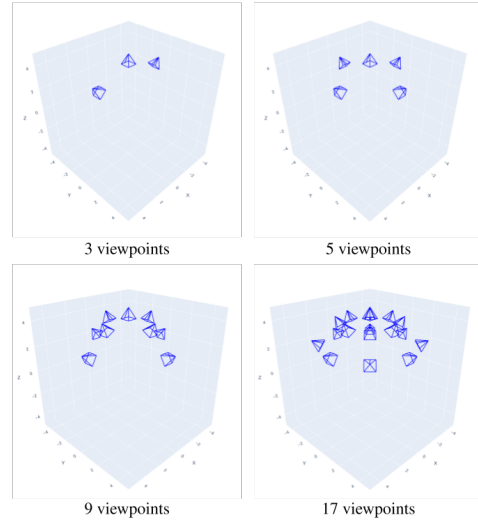


Figure 3. The four viewpoint collections designed for 2DGS training. These sets were constructed to evaluate the sensitivity of the baseline to viewpoint quality and sparsity

was used to model the scenes by attaching each tag as a texture to a 2×2 plane and rendering images from the pre-defined viewpoints.

Evaluation Metrics. For evaluation, we assess the readability of the rasterized 2D Gaussian Fitted tags by measuring the maximum viewing angle at which the QR code remains decodable from a fixed distance and azimuth. We also report standard Novel view synthesis metrics, that is PSNR/SSIM/LPIPS, one 20 randomly selected test viewpoints. In addition, we measure the time required to generate the primitives and the total number of primitives produced. The goal of these metrics to show how our method can yield comparable, if not better results to trained methods with a major reduction on inference time and memory footprint through a reduction in gaussian primitives count.

Implementation Details. We implement the fiducial marker pipeline using Shapely and NumPy. For rasterization, we employ the off-the-shelf 2D Gaussian splatting rasterizer by Huang *et al.* [15], and unless stated otherwise, the same hyperparameters are used for training all comparison baselines. Training is performed for 7,000 iterations on an RTX A6000 GPU. All rasterizations are likewise executed on this GPU to ensure fairness.

4.2. Results

Runtime and Primitive Count We report the average number of Gaussian primitives generated by each method across marker categories, along with the corresponding

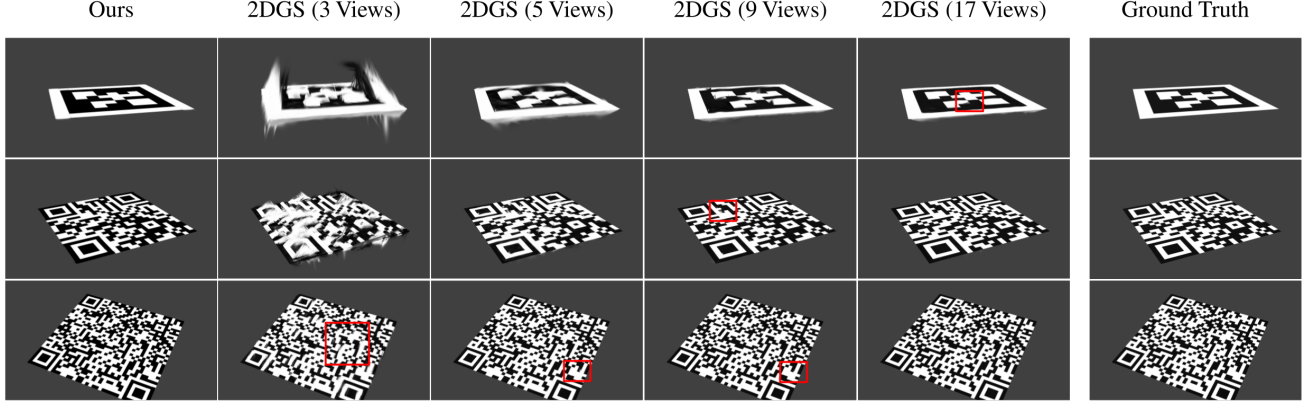


Figure 4. **Qualitative results of rasterized fiducial markers and QR codes under varying viewpoints.** Our rectangular Gaussian approximation produces stable and sharp renderings, while baseline methods exhibit artifacts such as blurring, distortions, or missing regions (highlighted in red).

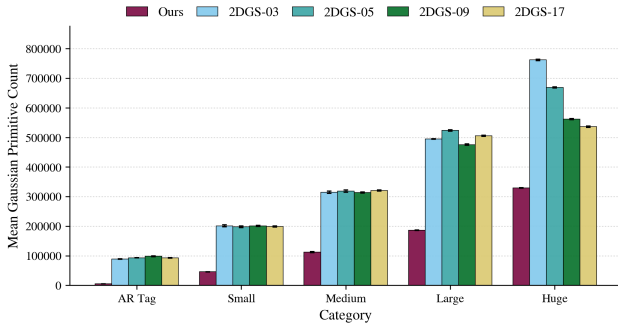


Figure 5. Mean Gaussian primitive counts across categories, showing our method achieves substantially lower counts than all 2DGS baselines.

Method	Mean Training time (s)
2DGS	
3 views	423
5 views	392
9 views	386
17 views	371
Ours (no training)	1.04

Table 2. Wall-clock comparison aggregated across categories. “Training” is technically a misnomer for **Ours**, which is an algorithmic construction without learning; we report its construction time to emphasize that results are effectively instantaneous relative to 2DGS.

runtime for training / primitive generation. As shown in Fig. 5, our method consistently achieves the lowest primitive counts across all categories, with the gap becoming

more pronounced as marker size increases. For instance, on HUGE markers, our approach reduces the primitive budget by more than 40% compared to the strongest 2DGS baseline. This reduction translates directly into faster inference, as fewer primitives must be rasterized at test time. Importantly, our method maintains readability while providing lower runtime overhead, highlighting its efficiency in both representation compactness and rendering cost. **Construction cost is likewise minimal:** as summarized in Table 2, 2DGS requires 423/392/386/371 s of training for 3/5/9/17 views, respectively, whereas our method performs no learning and completes primitive construction in 1.04 s. This is a $\sim 380\times$ reduction in setup time and, together with the smaller primitive budget, yields faster test-time rendering without sacrificing readability.

Image Quality and Readability In terms of readability, we demonstrate that our method outperforms the baseline even with more dense views (Table 3), and at a fraction of the number of Gaussian primitives involved. Note that, as QR complexity increases, the readability of our method continues to improve, which also suggests that algorithms that perform localization using AR tags would have no trouble here since they operate on the same grid-structured, high-contrast cues as QR codes.

It might be surprising to report mixed results in classical image quality metrics (Table 4); however, this is expected because 2DGS is trained directly on photographs and, in our setup, is exposed to views that are very similar to the test frames. As a result, 2DGS is optimized to reproduce the captured pixels and thus attains higher PSNR/SSIM when many views are available. Our approach, in contrast, never uses the images during optimization and reconstructs

QR Category	Ours		2DGS (3 Views)		2DGS (5 Views)		2DGS (9 Views)		2DGS (17 Views)	
	$\theta_{\text{det}} (^{\circ}) \uparrow$	$\theta_{\text{decode}} (^{\circ}) \uparrow$	$\theta_{\text{det}} (^{\circ})$	$\theta_{\text{decode}} (^{\circ})$	$\theta_{\text{det}} (^{\circ})$	$\theta_{\text{decode}} (^{\circ})$	$\theta_{\text{det}} (^{\circ})$	$\theta_{\text{decode}} (^{\circ})$	$\theta_{\text{det}} (^{\circ})$	$\theta_{\text{decode}} (^{\circ})$
small	80.0	80.0	73.8	60.0	79.4	68.2	81.6	75.4	81.0	79.0
medium	81.4	81.2	76.8	59.0	80.4	68.0	81.6	76.6	81.8	75.2
large	82.0	81.8	77.8	58.0	80.0	67.2	82.0	77.8	82.2	76.6
huge	84.0	82.2	77.8	56.8	79.4	65.4	82.2	72.0	82.6	75.4

Table 3. **Maximum detection and decoding angles (in degrees).** We report the maximum angle θ at which markers remain detectable (θ_{det}) and decodable (θ_{decode}). The proposed method consistently yields higher angles across all QR categories, with stronger gains in decoding robustness. Best results are highlighted in bold.

Category	Ours			2DGS (3 Views)			2DGS (5 Views)			2DGS (9 Views)			2DGS (17 Views)		
	PSNR \uparrow	SSIM \uparrow	LPIPS \downarrow	PSNR	SSIM	LPIPS	PSNR	SSIM	LPIPS	PSNR	SSIM	LPIPS	PSNR	SSIM	LPIPS
AR Tag	27.97	0.83	0.05	18.41	0.90	0.12	30.38	0.98	0.04	35.03	0.99	0.02	38.70	0.99	0.02
QR Small	25.41	0.83	0.05	19.86	0.90	0.12	26.90	0.96	0.04	33.82	0.99	0.02	37.21	0.99	0.02
QR Medium	23.58	0.84	0.06	19.64	0.89	0.12	26.97	0.96	0.04	33.52	0.99	0.02	36.10	0.99	0.02
QR Large	21.25	0.85	0.10	20.74	0.90	0.11	27.83	0.97	0.03	33.02	0.99	0.02	34.88	0.99	0.02
QR Huge	18.80	0.88	0.08	20.62	0.91	0.09	27.33	0.97	0.03	31.04	0.99	0.02	32.52	0.99	0.02

Table 4. **Novel View Synthesis** We report PSNR/SSIM/LPIPS for our method and for 2DGS trained with 3/5/9/17 views. Because 2DGS is trained on photographs and sees views highly similar to the test frames, its per-pixel metrics improve markedly with more views. Our method never uses the images and reconstructs the symbolic code layout, so photometric scores are lower, yet it is optimized for machine readability (cf. decoding results) and operates at a fraction of the compute/primitive budget. Best numbers are in bold.

the signal from symbolic structure, so per-pixel colors and shading may differ from the input photos even when the underlying bit layout is correct. Pixel-wise metrics penalize these benign deviations, while the decoding and detection angles reflect what matters for this task: machine readability under foreshortening, where our method is consistently stronger. Importantly, these gains are achieved without any training and at a fraction of the compute and memory cost, indicating that we deliver better task performance than training-based reconstruction despite a lower photometric similarity.

4.3. Greenhouse Simulation

In this section, we demonstrate how our fiducial marker splatting framework can be transferred to radiance field scenes for robotics simulation. As a proof of concept, we construct a greenhouse environment using 2D Gaussian splats trained from real images of a cucumber greenhouse. Individual splats are generated from these images and then stitched together to form a coherent miniature greenhouse scene, shown in Figure 6. In Gazebo simulations, using the fiducial markers, a mobile robot could effectively localize in the environment. This prototype highlights the potential of our approach for building lightweight, splat-based environments that can serve as testbeds for robotic perception and control.

5. Conclusion

We introduced a method for representing fiducial markers with Gaussian primitives that avoids reliance on splatting-based training. Our approach combines rectangle approximation with minimal rectilinear partitioning to produce



Figure 6. **Top:** Greenhouse Simulation Environment with 2D Gaussian Splatting. **Bottom:** Greenhouse Simulation with Fiducial Marker Splatting

compact representations that preserve readability while significantly reducing primitive counts. Experiments show that this reduction lowers runtime and inference cost, with the benefits becoming more pronounced as marker size increases.

As future work, we plan to extend this idea beyond rectangles, enabling Gaussian primitives to represent arbitrary shapes such as vector drawings. This would broaden the scope of our framework to structured visual representations beyond fiducial markers.

References

- [1] Jonathan T. Barron, Ben Mildenhall, Matthew Tancik, Peter Hedman, Ricardo Martin-Brualla, and Pratul P. Srinivasan. Mip-nerf: A multiscale representation for anti-aliasing neural radiance fields. *ICCV*, 2021. 2
- [2] Jonathan T. Barron, Ben Mildenhall, Dor Verbin, Pratul P. Srinivasan, and Peter Hedman. Mip-nerf 360: Unbounded anti-aliased neural radiance fields. *CVPR*, 2022. 2
- [3] Angel Chang, Angela Dai, Thomas Funkhouser, Maciej Halber, Matthias Niessner, Manolis Savva, Shuran Song, Andy Zeng, and Yinda Zhang. Matterport3d: Learning from rgb-d data in indoor environments. *International Conference on 3D Vision (3DV)*, 2017. 2
- [4] David Charatan, Sizhe Li, Andrea Tagliasacchi, and Vincent Sitzmann. pixelsplat: 3d gaussian splats from image pairs for scalable generalizable 3d reconstruction. In *CVPR*, 2024. 2
- [5] Timothy Chen, Ola Shorinwa, Joseph Bruno, Aiden Swann, Javier Yu, Weijia Zeng, Keiko Nagami, Philip Dames, and Mac Schwager. Splat-Nav: Safe Real-Time Robot Navigation in Gaussian Splatting Maps. *IEEE Transactions on Robotics*, 41:2765–2784, 2025. 2
- [6] Yuedong Chen, Haoifei Xu, Chuanxia Zheng, Bohan Zhuang, Marc Pollefeys, Andreas Geiger, Tat-Jen Cham, and Jianfei Cai. MVSplat: Efficient 3D Gaussian Splatting from Sparse Multi-view Images. In *Computer Vision – ECCV 2024*, pages 370–386, Cham, 2025. Springer Nature Switzerland. 2
- [7] Phillippe de Reffye, Claude Edelin, Jean Françon, Marc Jaeger, and Claude Puech. Plant models faithful to botanical structure and development. In *Proceedings of the 15th annual conference on Computer graphics and interactive techniques*, pages 151–158, New York, NY, USA, 1988. Association for Computing Machinery. 3
- [8] Xiang Feng, Wen Jie Liang, Hai Zhou Chen, Xiao Yu Liu, and Fang Yan. Autonomous Localization and Navigation for Agricultural Robots in Greenhouse. *Wireless Personal Communications*, 131(3):2039–2053, 2023. 1
- [9] L Ferrari, P.V Sankar, and J Sklansky. Minimal rectangular partitions of digitized blobs. *Computer Vision, Graphics, and Image Processing*, 28(1):58–71, 1984. 5, 1
- [10] Giuseppe Fragapane, Hans-Henrik Hvolby, Fabio Sgarbossa, and Jan Ola Strandhagen. Autonomous Mobile Robots in Hospital Logistics. In *Advances in Production Management Systems. The Path to Digital Transformation and Innovation of Production Management Systems*, pages 672–679, Cham, 2020. Springer International Publishing. 1
- [11] Steven J. Gortler, Radek Grzeszczuk, Richard Szeliski, and Michael F. Cohen. The lumigraph. In *Proceedings of the 23rd Annual Conference on Computer Graphics and Interactive Techniques*, pages 43–54, New York, NY, USA, 1996. Association for Computing Machinery. 2
- [12] Antoine Guédon and Vincent Lepetit. SuGaR: Surface-Aligned Gaussian Splatting for Efficient 3D Mesh Reconstruction and High-Quality Mesh Rendering. *2024 IEEE/CVF Conference on Computer Vision and Pattern Recognition (CVPR)*, pages 5354–5363, 2024. 2
- [13] Suman Harapanahalli, Niall O Mahony, Gustavo Velasco Hernandez, Sean Campbell, Daniel Riordan, and Joseph Walsh. Autonomous Navigation of mobile robots in factory environment. *Procedia Manufacturing*, 38:1524–1531, 2019. 1
- [14] Radim Hercik, Radek Byrtus, Rene Jaros, and Jiri Koziorek. Implementation of Autonomous Mobile Robot in SmartFactory. *Applied Sciences*, 12(17):8912, 2022. Number: 17 Publisher: Multidisciplinary Digital Publishing Institute. 1
- [15] Binbin Huang, Zehao Yu, Anpei Chen, Andreas Geiger, and Shenghua Gao. 2d gaussian splatting for geometrically accurate radiance fields. In *SIGGRAPH 2024 Conference Papers*. Association for Computing Machinery, 2024. 2, 3, 5
- [16] Antun Ivanovic, Marsela Polic, Jelena Tabak, and Matko Orsag. Render-in-the-loop Aerial Robotics Simulator: Case Study on Yield Estimation in Indoor Agriculture. In *2022 International Conference on Unmanned Aircraft Systems (ICUAS)*, pages 787–793, 2022. 2
- [17] Nilay Jadav, Harsh Chhajer, Upesh Patel, Devesh Jani, and Aum Barai. AI-Enhanced Quad-Wheeled Robot for Targeted Plant Disease Surveillance in Greenhouses. In *2023 Global Conference on Information Technologies and Communications (GCITC)*, pages 1–7, 2023. 1
- [18] Bernhard Kerbl, Georgios Kopanas, Thomas Leimkühler, and George Drettakis. 3d gaussian splatting for real-time radiance field rendering. *ACM Transactions on Graphics*, 42(4), 2023. 2
- [19] O. Kniemeyer, G. Buck-Sorlin, and W. Kurth. GroIMP as a platform for functional-structural modelling of plants. *Frontis*, pages 43–52, 2007. 3
- [20] N. Koenig and A. Howard. Design and use paradigms for Gazebo, an open-source multi-robot simulator. In *2004 IEEE/RSJ International Conference on Intelligent Robots and Systems (IROS)*, pages 2149–2154 vol.3, 2004. 1
- [21] N. Vimal Kumar and C. Selva Kumar. Development of collision free path planning algorithm for warehouse mobile robot. *Procedia Computer Science*, 133:456–463, 2018. 1
- [22] Marc Levoy and Pat Hanrahan. Light field rendering. In *Proceedings of the 23rd Annual Conference on Computer Graphics and Interactive Techniques*, pages 31–42, New York, NY, USA, 1996. Association for Computing Machinery. 2
- [23] Xinhai Li, Jialin Li, Ziheng Zhang, Rui Zhang, Fan Jia, Tiancai Wang, Haoqiang Fan, Kuo-Kun Tseng, and Ruiping Wang. RoboGSim: A Real2Sim2Real Robotic Gaussian Splatting Simulator, 2024. 2

- [24] Aristid Lindenmayer. Mathematical models for cellular interactions in development I. Filaments with one-sided inputs. *Journal of Theoretical Biology*, 18(3):280–299, 1968. 3
- [25] Zhen Liu, Yao Feng, Michael J. Black, Derek Nowrouzezahrai, Liam Paull, and Weiyang Liu. Meshdiffusion: Score-based generative 3d mesh modeling. In *International Conference on Learning Representations*, 2023. 2
- [26] Mohd Saiful Azimi Mahmud, Mohamad Shukri Zainal Abidin, Zaharuddin Mohamed, Muhammad Khairie Idham Abd Rahman, and Michihisa Iida. Multi-objective path planner for an agricultural mobile robot in a virtual greenhouse environment. *Computers and Electronics in Agriculture*, 157:488–499, 2019. 1
- [27] Ben Mildenhall, Pratul P. Srinivasan, Matthew Tancik, Jonathan T. Barron, Ravi Ramamoorthi, and Ren Ng. Nerf: Representing scenes as neural radiance fields for view synthesis. In *ECCV*, 2020. 2
- [28] Thomas Müller, Alex Evans, Christoph Schied, and Alexander Keller. Instant neural graphics primitives with a multiresolution hash encoding. *ACM Trans. Graph.*, 41(4):102:1–102:15, 2022. 2
- [29] Edwin Olson. AprilTag: A robust and flexible visual fiducial system. In *2011 IEEE International Conference on Robotics and Automation*, pages 3400–3407, 2011. 3, 5
- [30] Peter E. Oppenheimer. Real time design and animation of fractal plants and trees. *SIGGRAPH Comput. Graph.*, 20(4):55–64, 1986. 3
- [31] Yaoqiang Pan, Hao Cao, Kewei Hu, Hanwen Kang, and Xing Wang. A Novel Perception and Semantic Mapping Method for Robot Autonomy in Orchards, 2023. 1
- [32] Christophe Pradal, Samuel Dufour-Kowalski, Frédéric Boudon, Christian Fournier, and Christophe Godin. OpenAlea: a visual programming and component-based software platform for plant modelling. *Functional plant biology: FPB*, 35(10):751–760, 2008. 3
- [33] William T. Reeves and Ricki Blau. Approximate and probabilistic algorithms for shading and rendering structured particle systems. *SIGGRAPH Comput. Graph.*, 19(3):313–322, 1985. 3
- [34] Johannes Lutz Schönberger and Jan-Michael Frahm. Structure-from-motion revisited. In *Conference on Computer Vision and Pattern Recognition (CVPR)*, 2016. 5
- [35] Yawar Siddiqui, Antonio Alliegro, Alexey Artemov, Tatiana Tommasi, Daniele Sirigatti, Vladislav Rosov, Angela Dai, and Matthias Nießner. MeshGPT: Generating Triangle Meshes with Decoder-Only Transformers. In *2024 IEEE/CVF Conference on Computer Vision and Pattern Recognition (CVPR)*, pages 19615–19625. IEEE Computer Society, 2024. 2
- [36] K. S. Suresh, R. Venkatesan, and S. Venugopal. Mobile robot path planning using multi-objective genetic algorithm in industrial automation. *Soft Computing*, 26(15):7387–7400, 2022. 1
- [37] Kosmas Tsiakas, Alexios Papadimitriou, Eleftheria Maria Pechlivani, Dimitrios Giakoumis, Nikolaos Frangakis, Antonios Gasteratos, and Dimitrios Tzovaras. An Autonomous Navigation Framework for Holonomic Mobile Robots in Confined Agricultural Environments. *Robotics*, 12(6):146, 2023. 1
- [38] Naoum Tsolakis, Dimitrios Bechtsis, and Dionysis Bochtis. AgROS: A Robot Operating System Based Emulation Tool for Agricultural Robotics. *Agronomy*, 9(7):403, 2019. 2
- [39] Hendrik Unger, Tobias Markert, and Egon Müller. Evaluation of use cases of autonomous mobile robots in factory environments. *Procedia Manufacturing*, 17:254–261, 2018. 1
- [40] Brent Van De Walker, Brendan Byrne, Joshua Near, Blake Purdie, Matthew Whatman, David Weales, Cole Tarry, and Medhat Moussa. Developing a Realistic Simulation Environment for Robotics Harvesting Operations in a Vegetable Greenhouse. *Agronomy*, 11(9):1848, 2021. 2
- [41] Jason Weber and Joseph Penn. Creation and rendering of realistic trees. In *Proceedings of the 22nd annual conference on Computer graphics and interactive techniques*, pages 119–128, New York, NY, USA, 1995. Association for Computing Machinery. 3
- [42] Zhirong Wu, Shuran Song, Aditya Khosla, Fisher Yu, Linguang Zhang, Xiaoou Tang, and Jianxiong Xiao. 3D ShapeNets: A deep representation for volumetric shapes. In *2015 IEEE Conference on Computer Vision and Pattern Recognition (CVPR)*, pages 1912–1920. IEEE Computer Society, 2015. 2
- [43] Yu Xiang, Roozbeh Mottaghi, and Silvio Savarese. Beyond PASCAL: A benchmark for 3D object detection in the wild. In *IEEE Winter Conference on Applications of Computer Vision*, pages 75–82, 2014. 2
- [44] Oh Wei Xuan, Hazlina Selamat, and Mohd Taufiq Muslim. Autonomous Mobile Robot for Transporting Goods in Warehouse and Production. In *Advances in Intelligent Manufacturing and Robotics*, pages 555–565, Singapore, 2024. Springer Nature. 1
- [45] Chandan Yeshwanth, Yueh-Cheng Liu, Matthias Nießner, and Angela Dai. Scannet++: A high-fidelity dataset of 3d indoor scenes. In *Proceedings of the International Conference on Computer Vision (ICCV)*, 2023. 2
- [46] Darío Fernando Yépez-Ponce, José Vicente Salcedo, Paúl D. Rosero-Montalvo, and Javier Sanchis. Mobile robotics in smart farming: current trends and applications. *Frontiers in Artificial Intelligence*, 6, 2023. Publisher: Frontiers. 1
- [47] Yuhang Zheng, Xiangyu Chen, Yupeng Zheng, Songen Gu, Runyi Yang, Bu Jin, Pengfei Li, Chengliang Zhong, Zeng-mao Wang, Lina Liu, et al. Gaussiangrasper: 3d language gaussian splatting for open-vocabulary robotic grasping. *arXiv preprint arXiv:2403.09637*, 2024. 2

Fiducial Marker Splatting for High-Fidelity Robotics Simulations

Supplementary Material

6. Minimum Rectilinear Partition Algorithm

As noted in the main text, we now explain the rectangulation algorithm we used; the method follows [9] and is not our contribution. The pseudo-code is given in Algorithm 1

Given a rectilinear polygon $P = (V, E)$ with possible interior rectilinear holes $\mathbf{H} = \{(V_i, E_i)\}_{i=1}^k$, we collect all concave vertices V_c from the outer boundary and the hole boundaries. From V_c we enumerate all valid axis-aligned chords—horizontal C_h and vertical C_v —that lie completely inside P . We then build a bipartite graph $G = (C_v, C_h, E_c)$ whose edges connect perpendicular chords that geometrically intersect. Computing a maximum bipartite matching M and the corresponding minimum vertex cover S (by König’s theorem) yields a maximum set of pairwise non-intersecting chords $I = (C_v \cup C_h) \setminus S$.

Drawing all chords in I partitions P into smaller rectilinear subpolygons \mathbf{P}_r with induced holes \mathbf{H}_r (Algorithm 1). Each subpolygon is then rectangulated by a greedy routine: starting from concave vertices not already incident to drawn chords, we insert maximal interior axis-aligned segments (extending until hitting an existing edge, a chord, or a hole boundary) and iterate until only rectangles remain. The union over subpolygons gives the final partition \mathbf{R} .

7. Additional Visualizations

We provide additional visualizations for two aspects: (i) extended qualitative comparisons with 2DGS (see Sec. 4); and (ii) a demonstration of incorporating and detecting AprilTags within a Gaussian Splatting greenhouse simulation. All results use the same AprilTag / QR code assets and training data as in the main paper— we only include additional views/images.

Algorithm 1 Minimum Rectilinear Partition

Input: Rectilinear polygon $P = (V, E)$, Interior rectilinear polygons $\mathbf{H} = \{(V_i, E_i)\}_{i=1}^k$.
Output: A minimum set of non-overlapping rectangles \mathbf{R} that partitions P .
 $V_c \leftarrow \text{CONCAVEVERTICES}(V, E)$
for $i \leftarrow 1, k$ **do**
 $V_c \leftarrow V_c \cup \text{CONCAVEVERTICES}(V_i, E_i)$
end for
 $C_h \leftarrow \text{AXISPARALLELCHORDS}(V_c, \text{axis} = (1, 0))$
 $C_v \leftarrow \text{AXISPARALLELCHORDS}(V_c, \text{axis} = (0, 1))$
 $E_c \leftarrow \{(c_i, c_j) \in C_h \times C_v : \text{INTERSECT}(c_i, c_j)\}$
 $G \leftarrow (C_v, C_h, E_c) \quad \triangleright \text{Bipartite Graph}$
 $M \leftarrow \text{MAXBIPARTITEMATCHING}(G)$
 $S \leftarrow \text{MINVERTEXCOVER}(G, M) \quad \triangleright \text{König’s Theorem}$
 $I \leftarrow (C_v \cup C_h) \setminus S$
 $\mathbf{P}_r, \mathbf{H}_r \leftarrow \text{PARTITION}(P, \mathbf{H}, I)$
 $\mathbf{R} \leftarrow \emptyset$
for $j \leftarrow 1, |\mathbf{P}_r|$ **do**
 $V_j, E_j \leftarrow \mathbf{P}_r[j]$
 $\mathbf{H}_j \leftarrow \mathbf{H}_r[j]$
 $\mathbf{R}_j \leftarrow \text{GREEDYPARTITION}((V_j, E_j), \mathbf{H}_j)$
 $\mathbf{R} \leftarrow \mathbf{R} \cup \mathbf{R}_j$
end for
return \mathbf{R}

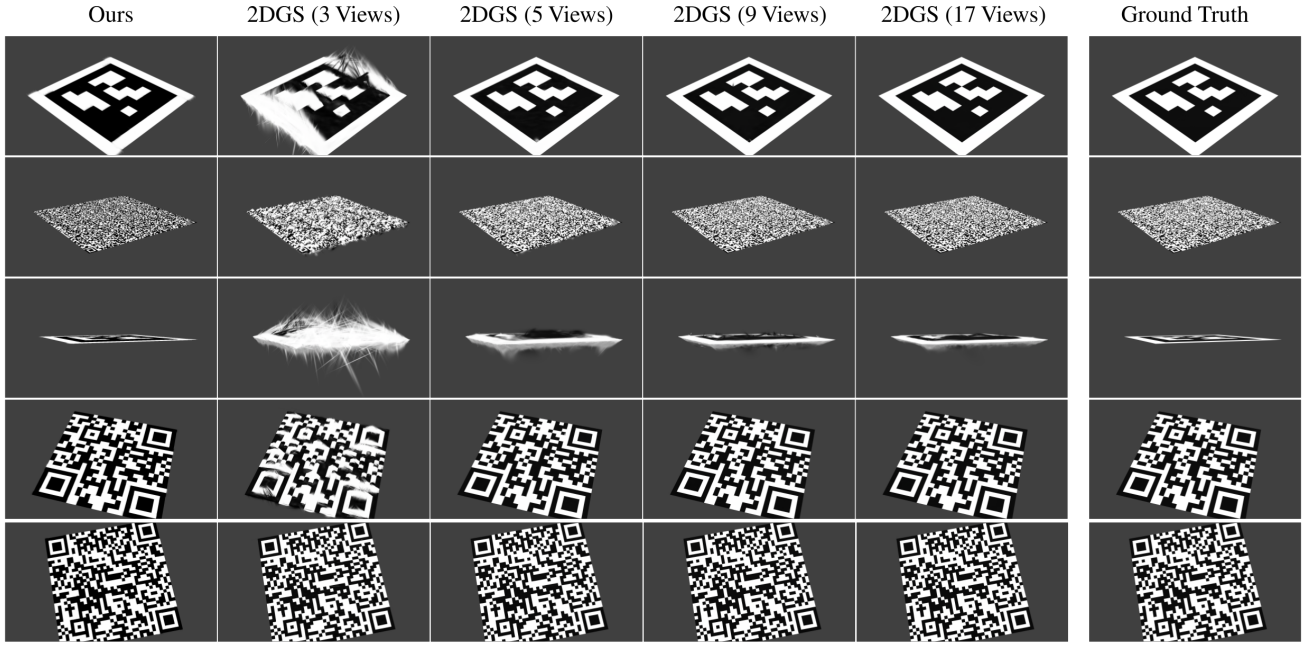


Figure 7. **Additional qualitative comparisons on planar fiducials.** Columns: Ours, 2DGS trained with 3/5/9/17 views, and Ground Truth. Under narrow training baselines (3–5 views), 2DGS degrades sharply—showing thickness/halo artifacts and texture distortions, especially at oblique viewpoints—improving only gradually with more views. Our method remains planar and crisp across viewpoints.

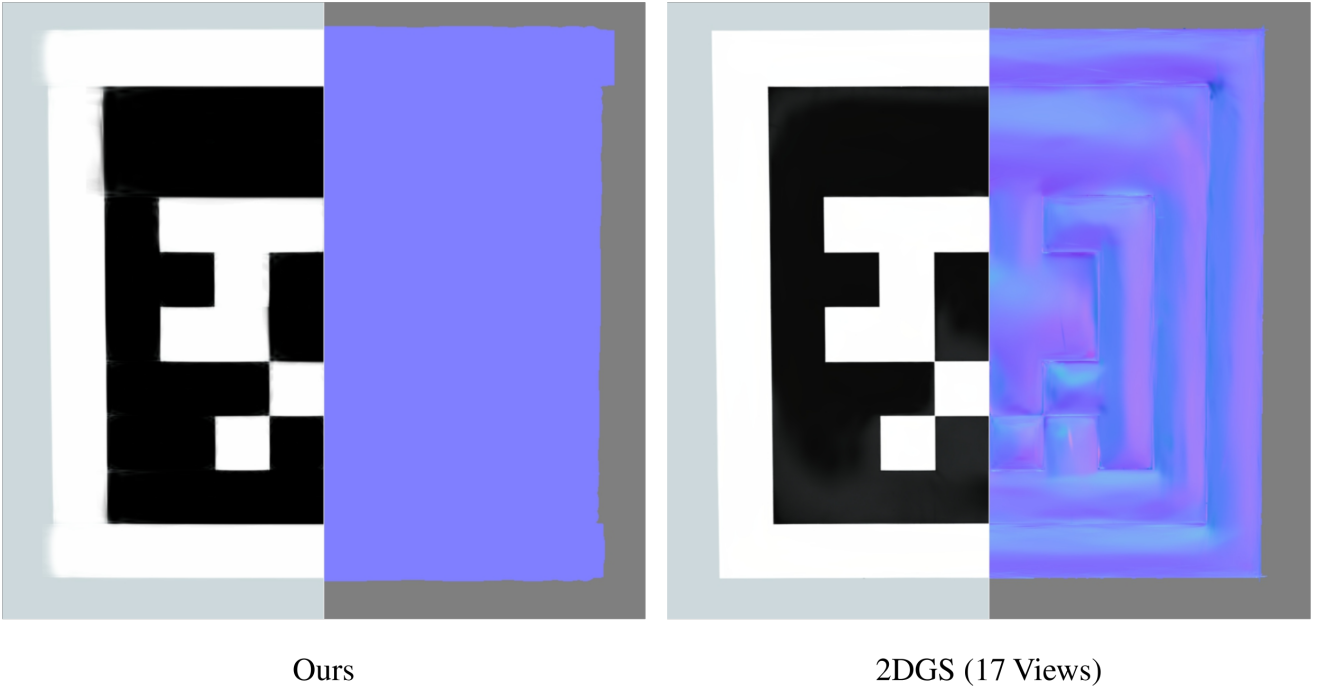
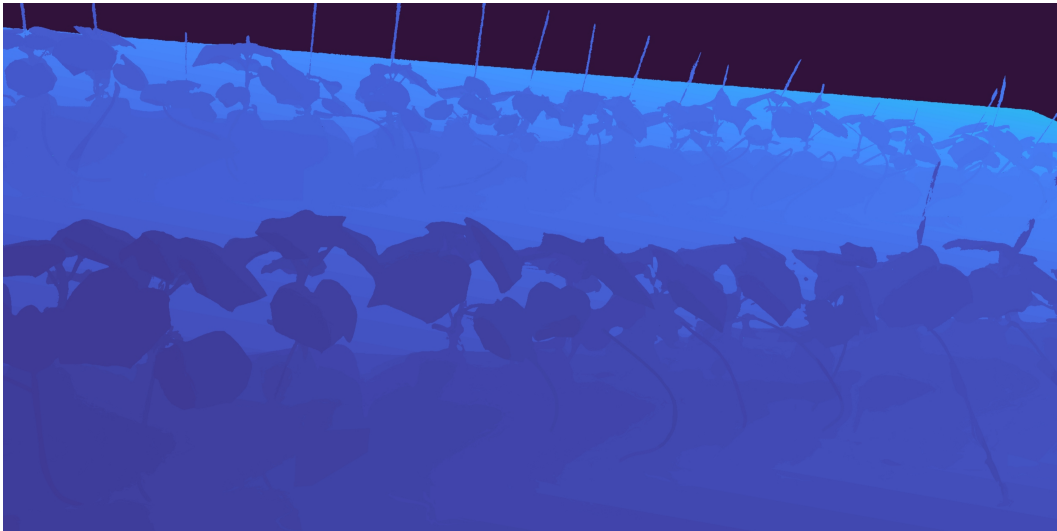


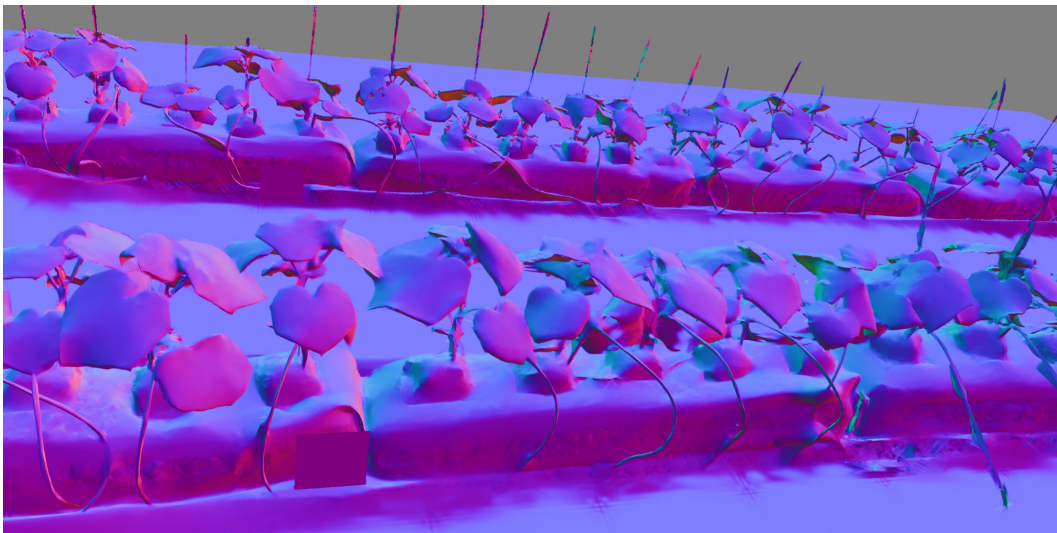
Figure 8. **Normal predictions on a planar AprilTag.** Each panel shows RGB (left half) and the estimated normal map (right half). Left: ours maintains a uniform planar normal. Right: 2DGS entangles texture with geometry, producing spurious relief where the tag pattern appears in the normals.



(a) AprilTag detections overlaid on the Gaussian Splatting greenhouse render.



(b) Depth map from the same viewpoint.



(c) Per-pixel surface normals (RGB) from the same viewpoint.

Figure 9. **Additional greenhouse visualizations:** (a) AprilTag detection overlay, (b) depth map, and (c) surface normals.